

Research Article

Analysis of the Dynamic Response in Blast-Loaded CFRP-Strengthened Metallic Beams

Zhenyu Wang,¹ Yang Zhao,² Xu Liang,¹ and Zhiguo He²

¹ College of Civil Engineering and Architecture, Zhejiang University, Hangzhou 310058, China

² Department of Ocean Science and Engineering, Zhejiang University, Hangzhou 310058, China

Correspondence should be addressed to Zhenyu Wang; wzyu@zju.edu.cn

Received 26 February 2013; Revised 30 May 2013; Accepted 4 June 2013

Academic Editor: Roham Rafiee

Copyright © 2013 Zhenyu Wang et al. This is an open access article distributed under the Creative Commons Attribution License, which permits unrestricted use, distribution, and reproduction in any medium, provided the original work is properly cited.

Carbon fiber-reinforced polymer composites (CFRPs) are good candidates in enhancing the blast resistant performance of vulnerable public buildings and in reinforcing old buildings. The use of CFRP in retrofitting and strengthening applications is traditionally associated with concrete structures. Nevertheless, more recently, there has been a remarkable aspiration in strengthening metallic structures and components using CFRP. This paper presents a relatively simple analytical solution for the deformation and ultimate strength calculation of hybrid metal-CFRP beams when subjected to pulse loading, with a particular focus on blast loading. The analytical model is based on a full interaction between the metal and the FRP and is capable of producing reasonable results in a dynamic loading scenario. A nonlinear finite element (FE) model is also developed to reveal the full dynamic behavior of the CFRP-epoxy-steel hybrid beam, considering the detailed effects, that is, large strains, high strain rates in metal, and different failure modes of the hybrid beam. Experimental results confirm the analytical and the FE results and show a strong correlation.

1. Introduction

The current increase in terrorist attacks directed towards vulnerable civil and military infrastructures, as well as accidental explosions occurring in various blast scenarios, may cause considerable and unprecedented levels of damage and loss of life. Thus, the blast resistance of existing structures, which are potentially prone to such threats, for example, vulnerable public buildings [1], needs to be enhanced. Additionally, some old buildings need to be reinforced, retrofitted, or strengthened against dynamic loads using efficient but nonconventional methods [2], such as using novel light-weight fibre-reinforced plastic (FRP) materials that show good strength and stiffness [3]. The use of carbon fiber-reinforced polymers (CFRPs) in retrofitting and strengthening applications has been increasing over the past few decades [4]. These materials, traditionally applied in conjunction with concrete structures [5–7], have more recently been applied to strengthen metallic structures [8–15]. Recently, increasingly more research is being conducted on strengthening metallic structures using CFRP composites due to the advantages CFRP offers such as high strength and light weight, as well as

the nonreactive and corrosion resistant properties [16] compared with the conventional construction materials.

Some literatures address the behavior of FRP-strengthened metallic structures subjected to static loads [17, 18]. Haedir et al. [19] studied steel circular hollow sections (CHSs) beams reinforced by CFRP sheets under pure bending; the tests revealed that the strength of the composite beams is influenced mainly by the amount of fiber reinforcement and the orientation of fibers. Youssef [20] provided an analytical model to describe the linear and nonlinear composite actions of hybrid steel/FRP-beams in the static load and validated it experimentally. In particular, CFRP has great potential to be used in retrofitting existing metallic structures as there is a minimum elastic mismatch between this class of FRPs and metals, thereby minimizing the bonding stresses thus limiting debonding, and various methods such as bolting and anchoring can be used to prevent the FRP from delamination and separation. To compare with the abundant studies on FRP-strengthened concrete structures, studies on analysis methods and mechanical properties of FRP-strengthened metallic structures are relatively few in number.

To date, few studies have looked into CFRP-metal hybrid beams subjected to dynamic loading. Bambach et al. [8] investigated the metal-FRP bond under impulsive loads by applying explosives to fully clamped solid aluminum beams. They showed that a significant amount of energy can be absorbed by the bonded CFRP, and the bonding of CFRP to the plastically deforming metallic structure provides the strengthening potential. Because the duration of the blast test is extremely short it is hard to measure the straining process of the beam and the detailed time history of strain at a particular point; hence to explore the detailed dynamic response of the hybrid beam and the damage evolution of each part is rendered difficult. Finite element analysis (FEA) provides an important methodology to capture the full dynamic behavior of the hybrid beam. FEA has been employed to validate the results of stress analysis for CFRP-steel hybrid beams by Deng et al. [21]. However, the steel and CFRP were considered to behave linearly. To date, few non-linear FE analyses have been conducted on the overall dynamic response of CFRP-strengthened beams that restrict gaining an insight into the mechanics of the FRP strengthened beams. Moreover, it is necessary to develop a simplified design method for engineering applications of FRP, while the literature does not have any examples of studies that analyze the analytical flexural capacity and permanent deformation of hybrid beams subjected to blast loads.

In this paper, a relatively simple analytical solution is presented for determining the deformation and ultimate capacity of hybrid beams strengthened with different layers of CFRP subjected to pulse loads, especially blast loads. Non-linear finite element analyses have also been conducted to reveal the dynamic behavior of the CFRP-epoxy-steel hybrid beam. In these FE analyses, blast loading is modeled as a uniformly distributed (spatially) rectangular pressure pulse (temporally). The well-known Johnson-Cook model is used to simulate metal (aluminum) subjected to large plastic strains and high strain rates, and the transversally isotropic elastic model along with the Hashin damage criterion is used to predict the damage of CFRP plies. Cohesive elements with direct traction versus separation formulation are used to simulate the bond between the metallic part and the FRP patch. The metal, CFRP, and epoxy are modeled by solid elements, shell elements, and cohesive elements, respectively. Moreover, different failure modes are taken into account in the FE analyses so that the method can replicate the actual situation. Comparisons to experimental results of Bambach et al. [8] confirm the analytical and FE results.

2. Analytical Modeling of the Dynamic Response for Blast-Loaded Hybrid Beams

The dynamic analysis procedure using an analytical model for hybrid beams subjected to blast loads consists of several steps: describing the basic assumptions of the analytical model, obtaining the mathematical model of the system, estimating the ultimate bending moment capacity of the CFRP-metal hybrid beam, and calculating the maximum and permanent deformation of the hybrid beam. When the beam is subjected to a given blast load, analyses for the dynamic response must

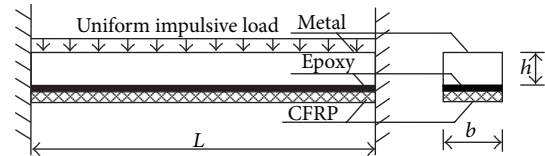


FIGURE 1: Schematic plot of hybrid beam.

be conducted. As in high-velocity impact and high-energy blast scenarios, one expects large deformation and plasticity; thus, considering the influence of the finite displacements and strain rate is necessary.

2.1. Fundamental Model Assumptions. Figure 1 shows the schematic of a CFRP-metal hybrid beam. The rectangle is the fundamental beam section shape, and the analysis method can be extended to I-section or tubular beam by proper modification. The explosive is applied as a cord of PETN in the tests [8] and is distributed as evenly as possible onto the beam. The explosive is uniformly distributed along the length and approximately across the width. Thus, the blast is simulated as a uniformly distributed pulse load, and carbon fiber is bonded to the metal beam by epoxy. The metallic part is assumed to exhibit elastic perfectly plastic characteristics, with the tensile and compressive yield stresses being equal (f_y). The CFRP is generally assumed to be an elastic brittle material with zero ductility.

The assumptions are as follows, in order. (1) The metal is elastic perfectly plastic, and the FRP is elastic brittle. (2) Fiber rupture is the dominant failure mode in the hybrid system. (3) Plane sections of the hybrid system remain plane subsequent to deformation, implying a perfect bond between the two materials and ignoring the deformation of the epoxy layer.

The first assumption is due to metals depicting elastic-plastic-hardening behavior with different degrees of hardening, which can be ignored in a conservative design. The fracture energy in composites is mainly due to the elastic part rather than the softening part, and a perfectly brittle assumption is slightly conservative.

As for the second assumption, one must bear in mind that three failure modes exist, which are as follows, in outline form: fiber rupture (FR), metal-fiber debonding (MFD), and interlaminar rupture/debonding (ILD), with fiber rupture occurring in almost every test, and thus being the prevalent failure mode. Metal is an elastic plastic material as stated in assumption (1), and the plastic strain of the metal is much larger than the failure strain of CFRP, so fiber rupture occurs prior to metal yielding. Thus, from experimental observations, FR is the main failure mode, thus constituting the second assumption.

The third assumption arises as a result of experimental observations. Schnerch and Rizkalla [4] and Deng et al. [22] showed that plane sections of the hybrid system remain plane subsequent to deformation in their models, and this assumption is also used in this paper. The CFRP and metal are bonded together by a thin epoxy layer. The thickness and strength of epoxy can be ignored compared with the metallic part and the FRP. The experimental results and

the FE analyses have demonstrated that debonding seldom occurs and that fiber breakage is the dominant failure mode in the hybrid beam; thus, the slip between the aluminum beam and the CFRP can be ignored at the interface.

2.2. Ultimate Bending Moment of a Hybrid Beam [22]. The maximum tensile strength of CFRP is written as

$$F_p = \varepsilon_{pu} E_p A_p, \quad (1)$$

where ε_{pu} is the ultimate strain of CFRP, E_p is the elastic modulus of CFRP, and A_p is the cross-sectional area of the CFRP patch.

When calculating the moment for a fully plastic cross-section, the neutral axis is located in the metal beam:

$$F_p + f_y b (h - \chi_c) = f_y b \chi_c, \quad (2)$$

where f_y is the tensile yield strength of metal, b is the width of the beam and h is the height of the cross section (depth of the beam) of the beam, and χ_c is the distance between the neutral axis and the top fiber of the beam. Hence, χ_c is given by

$$\chi_c = \frac{F_p + f_y b h}{2 f_y b}. \quad (3)$$

The ultimate bending moment of the hybrid beam can be thus written as

$$M_u = F_p (h - \chi_c) + \frac{f_y b (h - \chi_c)^2 + f_y b \chi_c^2}{2}. \quad (4)$$

2.3. The Permanent Deformation of the Hybrid Beam. Mathematically speaking, external overpressure pulse loadings with a finite impulse of infinitely large magnitude and an infinitesimally short duration are known as impulsive, and Dirac's delta function is used to describe this behavior. In a practical engineering problem, when the ratio of the load duration to the first natural period is less than a certain threshold, here 0.1, the pulse is known as an impulse. When the fully clamped beam is loaded impulsively, the permanent deflection W_f is given by an expression given by Jones [23] with the rigid plastic method and assuming all the external energy was absorbed through plastic deformation. The permanent deflection can be written as follows:

$$\frac{W_f}{h} = \frac{\lambda}{6}, \quad (5)$$

where

$$\lambda = \frac{m V_0^2 L^2}{M_u h}. \quad (6)$$

In (6), m is the beam mass/unit length, L is the beam length, V_0 is the initial uniform transverse velocity corresponding to an impulsive load, and M_u is the ultimate bending moment of hybrid beam. As these calculations are performed within the framework of rigid plasticity, there is no distinction between the maximum and permanent displacements.

2.4. Influence of Finite Displacements. When the beam is fully clamped due to the conservation of energy [24] one can write

$$\int_A (p - \mu \ddot{w}) \dot{w} dA = \sum_{m=1}^r \int_{l_m} (M + Nw) \dot{\theta}_m l_m, \quad (7)$$

where p is the pressure and μ is the mass per unit length of beam.

The conservation of energy is used to describe the influence of the finite displacements, and the final permanent deflection, as given by Jones [23], results in the permanent displacement of a fully clamped beam subjected to a uniformly distributed pressure pulse being written as

$$\frac{W_f}{h} = \frac{[(1 + 3\lambda/4)^{1/2} - 1]}{2}, \quad (8)$$

where λ is defined by (6).

2.5. Influence of Strain Rate. Cowper and Symonds' model is a well-known constitutive equation for strain-rate-sensitive behavior of metals, and Cowper and Symonds [25] suggested the following constitutive equation as a way to introduce strain-rate-sensitive behavior into metals:

$$\frac{\sigma_{0'}}{\sigma_0} = 1 + \left(\frac{\dot{\epsilon}}{D} \right)^{1/q}, \quad \sigma_{0'} \geq \sigma_0, \quad (9)$$

where $\sigma_{0'}$ is the dynamic stress at a uniaxial total strain rate, $\dot{\epsilon}$, σ_0 is the associated static flow stress, and D and q are constants of the particular material.

Taking the influence of strain rate into account, (8) becomes

$$\frac{W_f}{h} = \frac{[(1 + 3\lambda/4n)^{1/2} - 1]}{2}, \quad (10)$$

where λ is defined by (6), and the strain rate parameter n is

$$n = \frac{\sigma_{0'}}{\sigma_0} = 1 + \left[\frac{V_0^2}{6\sqrt{2}DL} \left(\frac{3\rho}{\sigma_0} \right)^{1/2} \right]^{1/q}. \quad (11)$$

The values of 6500 s^{-1} and 4 for D and q are assumed for aluminum [26].

3. Finite Element Modeling of Beams Strengthened with CFRP Subjected to a Transverse Blast Load

3.1. Blast Load Description. The studies by Jama et al. [27] have shown negligible influence of the assumed shape of the pressure pulse on the ultimate deformation; therefore, the blast wave was modeled as a spatially and temporally uniform rectangular pressure pulse distributed over the top flange of the beam along the span and across the breadth [28]. Nurick and his coworkers [29–31] have conducted extensive research on modeling blast loading using the blast chamber facilities. The amplitude of the pulse can be calculated based on total impulse as follows:

$$P = \frac{I}{A\tau}, \quad (12)$$

where I is the measured impulse ($N \cdot s$), A is the area of the top flange of the beam (mm^2), and τ is the duration of the blast (s).

3.2. Constitutive Modeling and Failure of the Metallic Part.

The Johnson-Cook model [32, 33] is a constitutive model for metals such as aluminum and steel subjected to large strains, high strain rates, and elevated temperatures. The model assumes a von Mises type yield criterion (J_2 -plasticity) and an isotropic strain hardening rule, such that the yield stress σ is composed of three parts and is expressed as

$$\sigma = (A + B\varepsilon^n)(1 + C \ln \dot{\varepsilon}^*) (1 - (T^*)^m), \quad (13)$$

where ε is the equivalent plastic strain, $\dot{\varepsilon}^* = \dot{\varepsilon}/\dot{\varepsilon}_0$ is the non-dimensional strain rate, $\dot{\varepsilon}$ is equivalent plastic strain rate, $\dot{\varepsilon}_0$ is a reference strain rate, and A, B, C, n, m are material parameters, with T^* being the non-dimensional temperature defined as

$$T^* = \frac{(T - T_0)}{(T_{\text{melt}} - T_0)}, \quad T_0 \leq T \leq T_{\text{melt}}, \quad (14)$$

where T is the current temperature in Kelvin, T_0 is the room temperature, and T_{melt} is the melting point temperature [34]. In (14), the first bracket represents an exponential strain hardening model, while the second and third brackets concern the effects of strain rate and temperature, respectively.

Johnson and Cook developed a fracture model [32] that is suitable for high strain rate deformation of metals. The commercial FE software ABAQUS provides a dynamic failure model specifically for the Johnson-Cook fracture model. This failure model is based on the value of the equivalent plastic strain at element integration points, and failure is assumed to occur when the damage parameter exceeds 1.0 [35]. The damage parameter, D_m , is a summation of equivalent plastic strain and the equivalent damage strain ratio and is defined as

$$D_m = \sum \frac{\Delta \varepsilon^p}{\bar{\varepsilon}_f^{\text{pl}}}, \quad (15)$$

where $\Delta \varepsilon^p$ is an increment of the equivalent plastic strain and $\bar{\varepsilon}_f^{\text{pl}}$ is the strain at failure and can be defined as:

$$\bar{\varepsilon}_f^{\text{pl}} = [D_1 + D_2 \exp(D_3 \sigma^*)] \left[1 + D_4 \ln \left(\frac{\dot{\varepsilon}^p}{\dot{\varepsilon}_0} \right) \right] \times \left(1 + D_5 \left(\frac{T - T_0}{T_{\text{melt}} - T_0} \right)^m \right), \quad (16)$$

where D_1 - D_5 are material constant identified from tests and σ^* is the dimensionless press stress ratio; it is defined as $\sigma^* = \sigma^m/\bar{\sigma}$, where σ^m is the average of the three normal stress and $\bar{\sigma}$ is the Mises equivalent stress [36].

3.3. Failure Model of CFRP. In ABAQUS, CFRP is modeled by shell elements that are used to model structures in which one dimension, the thickness, is significantly smaller than the

other dimensions [35]. ABAQUS offers a damage model to predict the onset of damage and to model damage evolution for elastic brittle materials (such as CFRP) with anisotropic behavior. The model is primarily intended to be used with fiber-reinforced materials because they typically exhibit such behavior.

This damage model requires a damage initiation criterion and a damage evolution rule.

Damage initiation refers to the onset of stiffness degradation of a material point where the first criterion is met. The methodology developed by Hashin [37] is suitable for finding the failure criteria of fiber-reinforced composites. The general form of the three-dimensional failure criterion for fiber-reinforced composites is approximated by a complete quadratic polynomial in terms of the non-dimensional basis in the 3D stress space [38]. These criteria consider four different damage initiation mechanisms [35].

Fiber tension ($\hat{\sigma}_{11} \geq 0$):

$$F_f^t = \left(\frac{\hat{\sigma}_{11}}{X^t} \right)^2 + \alpha \left(\frac{\hat{\tau}_{12}}{S^L} \right)^2. \quad (17)$$

Fiber compression ($\hat{\sigma}_{11} < 0$):

$$F_f^c = \left(\frac{\hat{\sigma}_{11}}{X^c} \right)^2. \quad (18)$$

Matrix tension ($\hat{\sigma}_{22} \geq 0$):

$$F_m^t = \left(\frac{\hat{\sigma}_{22}}{Y^t} \right)^2 + \left(\frac{\hat{\tau}_{12}}{S^L} \right)^2. \quad (19)$$

Matrix compression ($\hat{\sigma}_{22} < 0$) [39]:

$$F_m^c = \begin{cases} \left(\frac{\tau_{\text{eff}}^{mT}}{S^T} \right)^2 + \left(\frac{\tau_{\text{eff}}^{mL}}{S_{is}^L} \right)^2 & \sigma_{11} < Y^c, \\ \left(\frac{\tau_{\text{eff}}^T}{S^T} \right)^2 + \left(\frac{\tau_{\text{eff}}^L}{S_{is}^L} \right)^2 & \sigma_{11} \geq Y^c, \end{cases} \quad (20)$$

where X^T is the longitudinal tensile strength, X^c is the longitudinal compressive strength, Y^T is the transverse tensile strength, Y^c is the transverse compressive strength, S^L is the longitudinal shear strength, S^T is the transverse shear strength, α is a shear stress coefficient, and $\hat{\sigma}_{11}, \hat{\sigma}_{22}, \hat{\tau}_{12}$ are the components of the effective stress tensor. The subscript "is" in (20) indicates that for general laminates the *in situ* longitudinal shear strength rather than the strength of a unidirectional laminate should be used; τ_{eff}^T and τ_{eff}^L are the effective shear stresses in both orthogonal directions; the superscript m indicates the misalignment coordinate frame.

The damage evolution response is combined with Hashin's damage initiation criteria and assumes that the damage is caused by the degradation of material stiffness, leading to material failure. CFRP is linearly elastic before damage initiation; thereafter, the response of the material can be computed based on the continuum damage mechanics averaging method, which allows for homogenization of

volumetric cracks and manifests all significant effects in a single damage parameter d (for each constituent):

$$\sigma = C_d \varepsilon, \quad (21)$$

$$C_d = \frac{1}{D} \begin{bmatrix} (1-d_f)E_1 & (1-d_f)(1-d_m)v_{21}E_1 & 0 \\ (1-d_f)(1-d_m)v_{12}E_2 & (1-d_m)E_2 & 0 \\ 0 & 0 & (1-d_s)GD \end{bmatrix}, \quad (22)$$

where $D = 1 - (1-d_f)(1-d_m)v_{12}v_{21}$, d_f reflects the current state of fiber damage, d_m reflects the current state of matrix damage, d_s reflects the current state of shear damage, E_1 is the intact (initial) Young's modulus in the fiber direction, E_2 is the Young's modulus in the direction perpendicular to the fibers, G is the shear modulus, and v_{12} and v_{21} are the in-plane Poisson's ratios. Due to transverse isotropy, only 5 independent parameters are required; hence, there is an interdependence among the elastic moduli and Poisson's ratios.

ABAQUS introduces a characteristic length to alleviate the mesh dependency during material softening, and the constitutive law can be expressed as a stress-displacement relation. As shown in Figure 2, OA is the stress-displacement curve prior to damage initiation, where point A is where CFRP failure begins. Thereafter, damage occurs along the line AC with the degradation of material stiffness until material failure. The evolution of damage is energy-based and is based on the following line integral (23), which signifies the amount of energy expended (dissipated as heat) in a cycle of loading-unloading (Figure 3). The modal fracture energies then determine when total separation has occurred in cases where mixed-mode loading is expected:

$$\oint_C \sigma_i d\delta_i = G_i, \quad (23)$$

where σ_i is the equivalent stress, δ_i is the equivalent displacement, and G_i is the fracture energy.

3.4. Constitutive Equation and Failure Model of Epoxy. The bond between the metal and CFRP can be modeled in many ways, for example, linear elastic fracture mechanics (LEFMs), crack tip open displacement (CTOD), and cohesive zone models (CZMs) [40, 41]. Compared with other methods, CZM provides advantages of dealing with tiny size of non-linear zone and being able to adequately predict the behavior of uncracked structures, including those with blunt notches, and not only the response of bodies with cracks [40]. Thus, the cohesive zone model is used to model the bond between the metal and CFRP.

ABAQUS [35] offers several methods to model the elastic-damage behavior of an adhesive and its failure. These methods include, but are not limited to, cohesive elements and surface-based cohesive behavior (cohesive interaction). These methods are based on the cohesive zone model and commonly used in modeling the delamination of interface failure, where crack paths are determined *a priori*. A cohesive element library encompasses elements to model the behavior

of adhesive joints, gaskets, and interfaces in composites. The constitutive response is commonly described in terms of a direct traction-separation law rather than a continuum model because the cohesive zone is very thin and may be considered to be of zero thickness, which takes into account variation of stress and strain through the thickness. The elastic behavior can then be written as

$$\mathbf{t} = \begin{Bmatrix} t_n \\ t_s \\ t_t \end{Bmatrix} = \begin{bmatrix} K_{nm} & K_{ns} & K_{nt} \\ K_{ns} & K_{ss} & K_{st} \\ K_{nt} & K_{st} & K_{tt} \end{bmatrix} \begin{Bmatrix} \varepsilon_n \\ \varepsilon_s \\ \varepsilon_t \end{Bmatrix} = \mathbf{K} \varepsilon, \quad (24)$$

where \mathbf{t} is the nominal traction stress vector and consists of one normal and two shear tractions: t_n , t_s , t_t .

When the stresses and/or strains satisfy certain damage initiation criteria, the process of degradation begins. There are several damage initiation criteria, such as the maximum nominal stress criterion, the maximum nominal strain criterion, and the quadratic nominal stress criterion. In this paper, the quadratic nominal stress criterion is used as the damage initiation criterion, which can be represented as

$$\left\langle \frac{t_n}{t_n^0} \right\rangle^2 + \left\{ \frac{t_s}{t_s^0} \right\}^2 + \left\{ \frac{t_t}{t_t^0} \right\}^2 = 1, \quad (25)$$

where t_n^0 , t_s^0 , and t_t^0 represent the tensile strength and shear strength of the epoxy, respectively. The symbol $\langle \cdot \rangle$ represents the Macaulay bracket:

$$\langle t_n \rangle = \begin{cases} t_n, & t_n \geq 0, \\ 0, & t_n < 0. \end{cases} \quad (26)$$

Any convex hyper-surface in the space of normalized (non-dimensional) stress components can be taken as a failure initiation locus because convexity implies that the first law of thermodynamics (which is the basis for fracture mechanics) holds.

A scalar damage variable D , which represents the overall damage in the material, is introduced into the damage evolution law to describe the rate at which the material stiffness is degraded. The range of D is from 0 to 1, with 0 representing the undamaged case and 1, the total separation. Once the relevant initiation criterion is reached, D monotonically

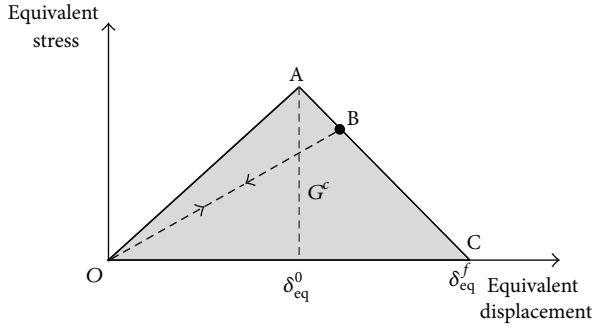


FIGURE 2: Equivalent stress versus equivalent displacement.

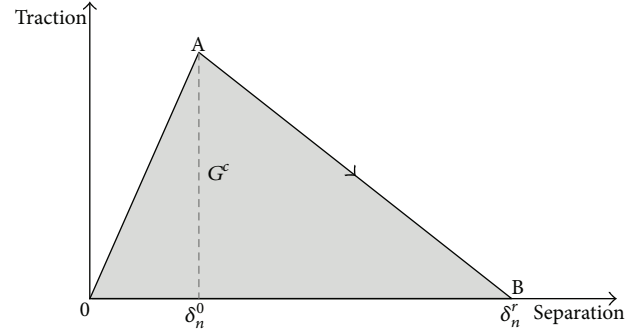


FIGURE 4: Linear damage evolution.

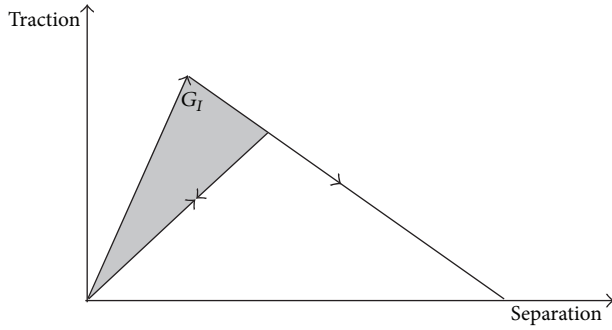


FIGURE 3: Damage evolution of CFRP.

evolves from 0 to 1 upon further loading. The corresponding stress components are then degraded as follows:

$$t_n = \begin{cases} (1-D)\bar{t}_n, & \bar{t}_n \geq 0 \\ \bar{t}_n, & \bar{t}_n < 0 \end{cases} \quad (\text{no damage to compressive stiffness}),$$

$$t_s = (1-D)\bar{t}_s,$$

$$t_t = (1-D)\bar{t}_t, \quad (27)$$

where \bar{t}_n , \bar{t}_s , and \bar{t}_t are the stress components predicted by multiplying the initial stiffness and the current relative displacements.

For the linear softening law (as shown in Figure 4), the damage index D can be expressed as

$$D = \frac{\delta_m^f (\delta_m^{\max} - \delta_m^0)}{\delta_m^{\max} (\delta_m^f - \delta_m^0)}, \quad (28)$$

where δ_m^{\max} is the maximum effective relative displacement attained during the loading history, δ_m^0 and δ_m^f are the effective relative displacement at the initiation and end of failure, respectively. The effective relative displacement δ_m can be written as

$$\delta_m = \sqrt{\langle \delta_n \rangle^2 + \delta_s^2 + \delta_t^2}. \quad (29)$$

Evaluation of the damage parameter depends upon the energy dissipated, which, in its own right, is a function

of the stress-strain characteristics. Thus, the formulation is circular, and the integration method determines whether the procedure is implicit or explicit. In this study, the explicit procedure is used throughout.

Surface-based cohesive behavior is primarily intended for situations in which the interface thickness is negligibly small. It assumes generalized traction-separation behavior which is very similar to cohesive elements that are defined using a traction-separation law. However, certain differences exist between these two methods. The main difference is that the interface thickness cannot be considered in the cohesive surface interaction formulation, while the thickness for the interface can be specified by requiring the initial constitutive thickness in the cohesive element. In this paper, cohesive elements are used to model the epoxy (adhesive) so that the influence of the epoxy thickness can be studied.

4. Experimental Study of Aluminum Beams Strengthened by CFRP

Bambach et al. [8] performed a total of 12 quasi-static tests and 58 impulsive tests on CFRP-strengthened aluminum beams subjected to blast loads. The impulsive tests were performed on clamped beams under an impulse resulting from explosives (Figure 5(b)). The explosive is applied as a cord of PETN and is distributed evenly on to the beam. Thus, the explosive is uniformly distributed on the beam, and the according impulse is also uniformly distributed. Two different grades of aluminum, namely, 6060-T5 and 6063-T6, were used in these tests, with nominal yield stresses of 110 MPa and 170 MPa, respectively. Figure 5(a) shows that the beams were all 25 mm wide and 500 mm long, while the exposed lengths were 300 mm. Three beam depths of 6 mm, 10 mm, and 12 mm were used (hereinafter to be referred to as 6 mm beam, 10 mm beam, and 12 mm beam, resp.). As shown in Figure 5(a), the CFRP patch was applied to the flexural tensile face of the beam (soffit plate) with a length of 300 mm. Araldite 420 epoxy was used to bond the CFRP and the aluminum. Three different fiber layouts (1, 3, and 5 layers) of CFRP were investigated and Araldite 420 epoxy was also used in between each layer. Three different fiber layouts (1, 3 and 5 layers) of CFRP were investigated, and Araldite 420 epoxy was also used in between each layer.

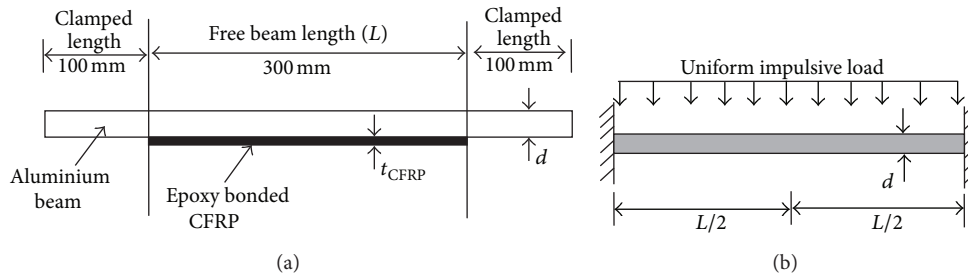


FIGURE 5: (a) A composite aluminum-CFRP beam specimen. (b) The idealized loading diagram [8].

The test results showed that the reduction of final deformation is evident both in static and impulsive tests with the increasing number of CFRP layers. In static tests, the three possible failure modes were fiber rupture (FR), metal-fiber debonding (MFD), and interlaminar rupture (ILD), while in impulsive tests, FR occurs in almost every specimen, while MFD only occurred in three specimens accompanied by FR. Additionally, most beams with 3 and 5 layers of CFRP suffered from ILD and FR, which is different from static tests. The tests also showed that a large amount of energy may be absorbed by the CFRP, while the effect might be reduced due to the fiber interlaminar debonding resulting from shock spalling which means a spallation arising from the intersection of rarefaction waves which cause tensile failure within the material [42].

5. Material Modeling and Elements

The aluminum beams were all 25 mm wide and 300 mm long, but had three different depths (6 mm, 10 mm, and 12 mm). Both sides of the beam were fixed, and the blast wave was simulated as a uniform rectangular pressure pulse distributed over the top flange of the beam. The widths and lengths of CFRP were the same as that of the aluminum beam in every case. In ABAQUS, the aluminum was modeled with solid elements (C3D8R). These are 8-noded generalized linear brick continuum elements with an hour-glass controlled algorithm and a reduced integration formulation implemented. The CFRP was modeled with 4-noded shell elements (S4R) with an hour-glass-controlled reduced integration formulation that allowed finite membrane strains. Epoxy was modeled with cohesive elements (COH3D8), which are 8-noded, three-dimensional cohesive elements with a direct traction-separation formulation that does not allow for a variation of stress/strain through the thickness. Epoxy can also be modeled by surface-based cohesive behavior. Surface-based cohesive behavior is defined as a surface interaction property with rigid-softening behavior, while the cohesive element is more realistic in its behavior as it allows for elastic deformation prior to the initiation of failure and has an elastic-damage softening behavior. These two methods are both valid in modeling the adhesive, with surface-based cohesive behavior being relatively simple and the cohesive element being more realistic. The material properties of the test specimens are tabulated in Table 1. The duration of the blast wave is calculated from the length of the beam and the velocity of

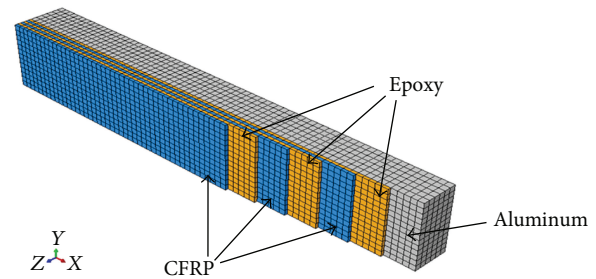


FIGURE 6: Schematic of a hybrid beam with three layers of CFRP.

detonation of explosive, and the blast wave velocity of 7500 m/s is used by Jama et al. [28].

The FE model simulates the hybrid beam as realistically as possible; so the assumptions of the analytical solution are not made for the FE model. Different failure models have been used for the different parts of the hybrid beam, as discussed previously. Figure 6 is the schematic of the hybrid beam with three layers of CFRP.

6. Results and Discussion

6.1. Comparison of Displacements

6.1.1. The Homogeneous Aluminum Beam. Figure 7 depicts a comparison of the three analysis methods for the homogeneous monolithic aluminum beam, where the horizontal axis represents the non-dimensionalized energy input that is parameter λ , and the vertical axis is the ratio of the permanent displacement to beam depth. As this figure suggests, given the variability experienced in testing with real explosives, the three methods agree overall very well. Although the analytical results over-predict displacement for higher blast energies, considering the assumption of elastic perfectly plasticity, the analytical solution is expected to over-predict the displacement results. The analysis above shows that the adopted constitutive model for aluminum, namely, the Johnson-Cook model is accurate in simulating the aluminum beam subjected to a blast load.

6.1.2. CFRP-Strengthened Beams. The results of the simple analytical solution are presented in Table 2. A number of groups of test data (15), which originate from Bambach's work, are available in the literature [8] and are listed in the

TABLE 1: Material properties [8, 21, 44].

Aluminum	Density (g/cm^3)	2.7	Poisson's ratio ν	0.33
	Elastic modulus E (GPa)	69		
Johnson-Cook model constants of aluminum (6063-T6)	A (MPa)	176.45	D_1	0.07413
	B (MPa)	63.99	D_2	0.0892
	n	0.07	D_3	-2.441
	C	0.0036	D_4	-4.76
	m	0	D_5	0
CFRP	Density (g/cm^3)	1.7	Shear modulus G_{23} (GPa)	3.7
	Thickness (mm)	0.176	Poisson's ratios, $\nu_{12} = \nu_{13}$	0.0058
	Elastic modulus E_1 (GPa)	240	Poisson's ratio, ν_{23}	0.25
	$E_2 = E_3$ (GPa)	10	Tensile strength, f_u (MPa)	3800
	Shear modulus $G_{12} = G_{13}$ (GPa)	26.5	Ultimate elongation, ϵ_f	1.55%
Epoxy	Density (g/cm^3)	1.1	Tensile strength, f_u (MPa)	35
	Thickness (mm)	—	Shear strength, f_u (MPa)	27
	Elastic modulus E (GPa)	1.85	Ultimate elongation, ϵ_f	3.4%

TABLE 2: Results of the three analysis methods for hybrid beams.

Beam depth, d/mm	Number	No. of CFRP layers	Initial velocity, $V_0/\text{m}\cdot\text{s}^{-1}$	Test results, W_f/mm	Analytical solutions, W_f/mm	FE analysis, W_f/mm	Relative error of analytical solution	Relative error of FEA
6	1	1	54	12.82	16.62	20.79	29.64%	62.17%
	2	1	63	20.98	19.81	26.12	-5.58%	24.50%
	3	3	50	10.76	13.38	11.81	24.35%	9.76%
	4	3	61	20.27	16.87	16.49	-16.77%	-18.65%
	5	5	46	7.80	11.41	10.65	46.28%	36.54%
	6	5	61	20.27	20.27	15.92	17.14	-21.46%
10	7	1	60	25.03	22.82	28.06	-8.83%	12.11%
	8	3	57	22.01	19.28	23.39	-12.40%	6.27%
	9	5	57	18.99	18.54	10.68	-2.37%	-43.76%
12	10	1	49	19.20	17.97	21.55	-6.41%	12.24%
	11	1	71	33.72	28.16	33.51	-16.49%	-0.62%
	12	3	47	18.00	14.89	13.11	-17.28%	-27.17%
	13	3	71	32.52	24.82	32.40	-23.68%	-0.37%
	14	5	50	17.16	15.57	11.74	-9.27%	-31.59%
	15	5	70	30.36	23.62	30.93	-22.20%	1.88%

table for comparison with the analytical solution and the FE results. The ratio of carbon fiber and epoxy mass is 1 : 3, and the initial velocity is in relative propinquity (from 46 m/s to 71 m/s) in these test data. Figure 8 shows the corroboration of the three different methods. As shown in this figure, the abscissa is the test results, and the ordinate is the result of the analytical solution and the FE analyses; the solid line depicts the test results, and the points are the results of the simple analytical solution and the FE analyses. This figure demonstrates that the points near the line correlate well with the test results, while the points further away from the corresponding experimental data have a weaker correlation. The points basically lie around the line, and there is some scatter in Figure 8; however, in view of the volatile nature of

a blast load, the agreement is considered satisfactory, and the trend is captured realistically.

The results above show that the permanent deformation calculated by the proposed analytical model and the numerical solution obtained from FEA agree overall with the test results, which demonstrates that the analytical solution is to be expected and is reasonably accurate. Thus, this solution can be used in the preliminary blast resistant assessment of this class of hybrid structures.

6.1.3. Error Analysis. Figure 8 demonstrates that the FE results are a little higher than the test results for 6 mm and 10 mm beams. Additionally, it is clear that the results of FEA for the 12 mm beams agree well with the test results. Table 2

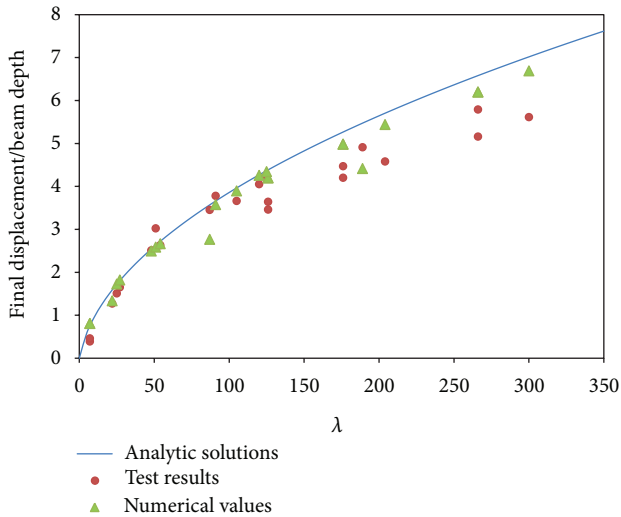


FIGURE 7: A comparison of different analysis methods for the aluminum beam.

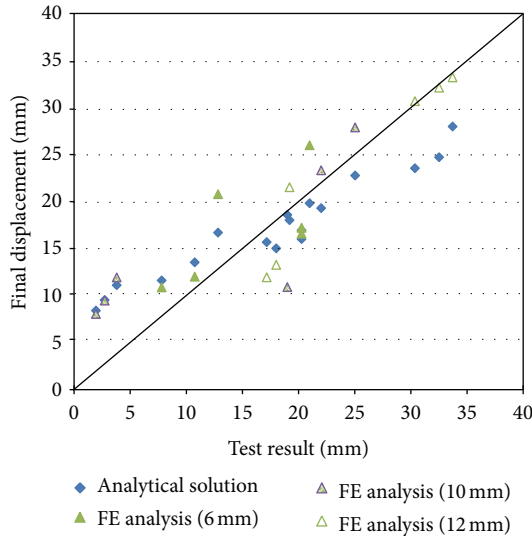


FIGURE 8: A comparison of the analytical solution, the numerical solution, and the test results.

also shows the relative error between the test results and the other two methods. There is a relative error in the results of the analytical solution and the FEA compared with those of the test results; nevertheless, considering the instability of the impact tests in general, these errors can be accepted. As mentioned before, FR is the failure criterion, and the bond between the CFRP and steel is assumed as a perfect bond in the analytical solution. In most specimens with FR failure, the analytical solution results have a good agreement with the FE results. However, for few specimens with MFD and ILD failure, debonding causes the error between the FE analysis and analytical solution. These errors will be solved in the future study by improving the analytical model.

Table 3 is the statistical average relative error of the FEA compared with the test results; this table demonstrates that

TABLE 3: Relative error statistics of FEA.

Depth of beam (mm)	Numbers of CFRP layers			
	0	1	3	5
	Relative error			
6	18.45%	43.34%	-4.45%	10.55%
10	3.34%	12.11%	6.27%	-43.76%
12	3.22%	5.81%	-13.77%	-14.86%

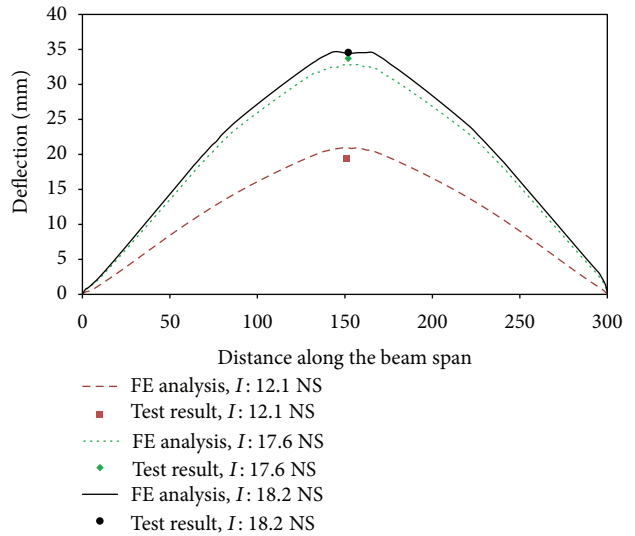


FIGURE 9: The distribution of deflection along the beam span for different impulses.

most of these results are accurate to within 19% except for the cases of 6 mm beam with 1 layer of CFRP and 10 mm beam with 5 layers of CFRP, resulting in relative errors of 43.34% and -43.76%, respectively. These errors may be a result of the instability in the impact tests conducted. More concrete data are required, along with an insight into the methodology of experiment, to be able to draw definitive conclusions in this regard.

6.2. Analysis of the Dynamic Response. Due to the very short duration of loading on a beam subjected to an explosion, it is difficult to obtain the data, such as stress, strain, and their time histories, accurately. Most experiments rely upon post-test observations of the amplitude of the permanent deformation and plastic strain. The numerical model developed in this paper can provide a tool to investigate the nonlinear damage process of hybrid beams.

6.2.1. Deflection of the Whole Hybrid Beam. Figures 9 and 10 show the deflection of the CFRP-aluminum hybrid beam under impulsive loads by the application of explosives. Figure 9 demonstrates the distribution of permanent deflection along the beam under different impulsive loads. The maximum deflection occurs at mid-span, and the maximum deflection of the test and the FEA agree well, both in position and in value. This observation is valid for cases where the ratio of the loading amplitude to the static plastic collapse

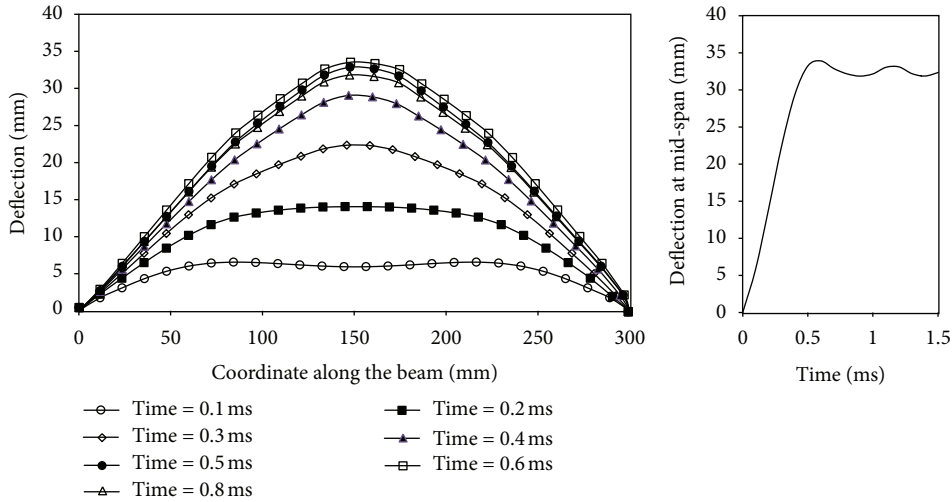


FIGURE 10: The deflection curve of a 12 mm aluminum beam subjected to an explosion.

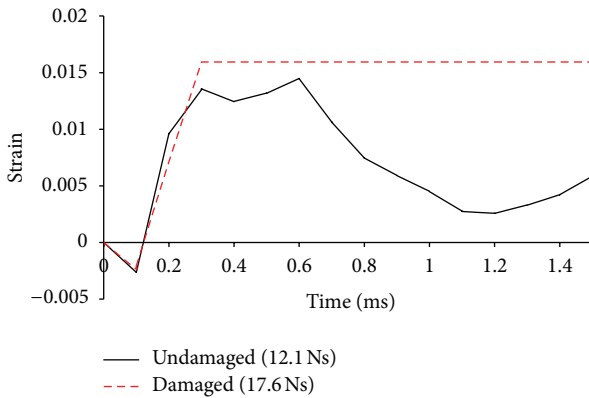


FIGURE 11: The strain evolution of the CFRP element at mid-span subjected to different impulses.

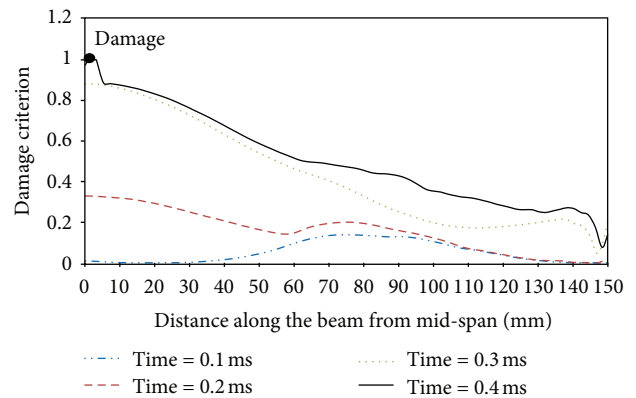


FIGURE 12: The damage evolution of the CFRP along the beam span for half of the beam.

load does not exceed 3. When this ratio goes beyond 3, there are two symmetrically poised travelling plastic hinges [43] at a finite distance that move toward one another and eventually meet in the middle of the beam. This case is fundamentally different from the case of the present study, as it involves a plasticized zone of finite length in the middle of the beam. The study of this case falls beyond the scope of the present work. Figure 10 shows the deflection development process for the hybrid beam subjected to an explosion; the left part of the figure indicates the spatial displacement profile along the beam, and the right part demonstrates the temporal evolution of the deflection at mid-span. The deflection reaches its peak value at about 0.6 ms and then undulates around the permanent deflection.

6.2.2. *Stress and Damage Analysis of CFRP.* Figure 11 indicates the strain in the CFRP at mid-span subjected to different impulses. The ultimate elongation is 1.55% in the studies conducted in this paper; thus, when the hybrid beam was subjected to an impulse of 17.6 Ns, the tensile strain of the soffit

CFRP patch reached 0.0155, which means it experienced damage. The distribution of the damage criterion along the right part of the beam is shown in Figure 12. Because of the inertia, at time 0.1 ms the beam between two hinges is not flat, and the stress is not zero (as shown in Figure 13). Therefore, the damage criterion is a minimal value but not zero at time 0.1 ms. At time 0.4 ms the damage criterion of the CFRP element around the mid-span reached 1.0, and the CFRP was fully damaged. Figure 13 indicates the development of tensile stress, where the horizontal axis denotes the right part of the beam, and the origin of horizontal axis is taken at the mid-span. The time interval 0.1 ms is a relatively long time interval and causes the stress jump between two stress curves, actually the stress is continuous if smaller time interval is adopted. It is evident from the figure that the tensile stress increased at the beginning to the point where the damage initiation criterion was met. The CFRP is an elastic brittle material, and the sudden rupture of CFRP at the mid-span causes the interfacial shear and normal stress concentrations at 0.3 ms. When the CFRP patch was damaged, the stress in the damaged

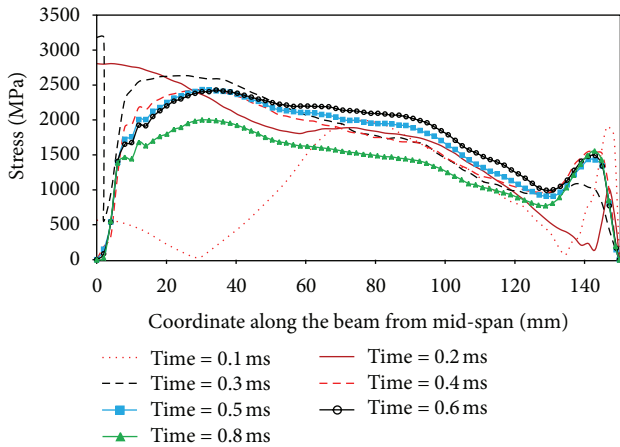


FIGURE 13: The stress curve of the CFRP along the beam by FEA.

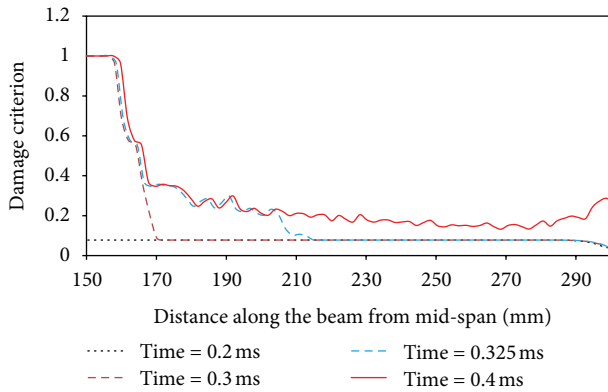


FIGURE 14: The distribution of the damage criterion for epoxy between CFRPs along the beam span.

region decreased to 0. If the damaged region expands from the mid-span to the end, the stress curve also moves in the same way.

6.2.3. Stress Analysis of Epoxy. As previously discussed, cohesive elements were used unanimously to model the epoxy, and the debonding is modeled by damage in the cohesive layer. The quadratic nominal stress-based damage initiation criterion is used throughout as the damage initiation criterion. When the damage criterion reaches 1.0, the damage is initiated. Subsequently, the cohesive damage is used, which is equivalent to the fracture energy-based models, to model the full separation. Figure 14 demonstrates the evolution of interlaminar debonding, with the cohesive element being damaged in the vicinity of the mid-span, which means that the debonding region is in the proximity of the mid-span. The figure also indicates that the debonding region is almost stationary and does not extend with time.

6.3. Failure Modes. In tests, there were 36 hybrid beams subjected to impulsive loading, and 34 beams were failed [8]. Concerning three failure modes, FR, MFD, and ILD, as previously discussed, FR was the most prevalent mode and

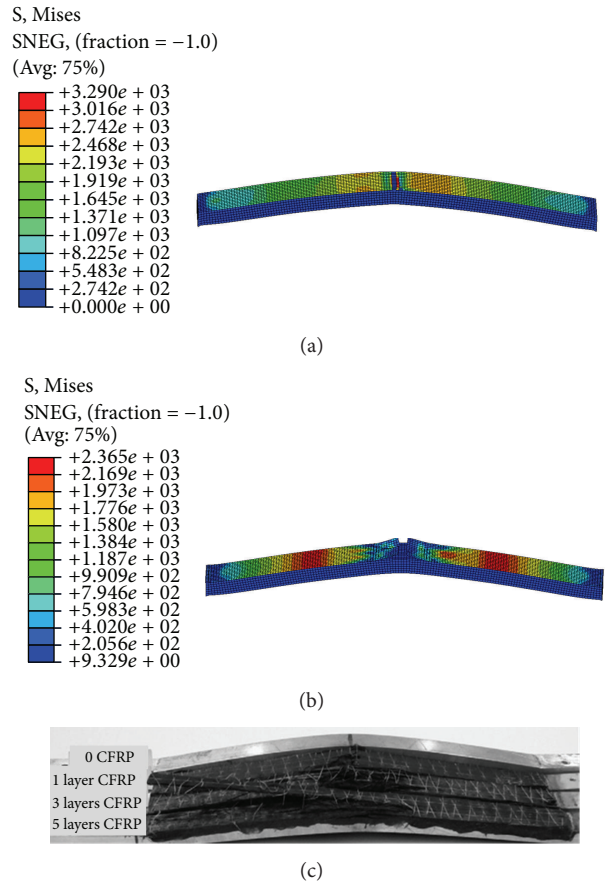


FIGURE 15: (a) Fiber rupture modeled by FEA. (b) Debonding and fiber rupture modeled by FEA. (unit: MPa) (c) Photos of the impulsive beam test results [8].

dominated all the 34 failure beams. Apart from 15 beams failed in only FR, which is shown in Figure 15(a) by FEA and can be seen from the beam with 1 layer CFRP in Figure 15(c), some beams failed with combined failure modes. 16 of them failed with FR and ILD, which is shown in Figure 15(b) by FEA and can be seen from the beam with 3 or 5 layers CFRP in Figure 15(c). Two of the other 3 beams failed with concerted actions of FR, ILD, and MFD, and the last beam failed with concerted actions of FR and MFD. In the FE simulation, FR was found in every specimen, and beams strengthened with 3 or 5 layers CFRP mostly failed by FR and ILD. No individual MFD failure mode occurred in FEA. The agreement of the FEA and tests is reasonably good.

7. Conclusions

In this paper, a simple analytical solution is proposed to calculate the deformation and ultimate load bearing capacity of CFRP-strengthened metal beams. An FE modeling scheme was developed to simulate the damage in hybrid metal-CFRP beams, that is, metallic beams strengthened with externally bonded soffit CFRP plates. Test results from the literature [8] were adopted to validate the proposed analytical solution and the FE simulation results, and the agreement between three

results obtained from different solution methods was found to be good, which demonstrates that the simple analytical solution and FE are relatively accurate and reliable.

Due to its prevalence in the failure modes, fiber rupture is considered as the criterion of structural failure in the simple analytical solution. This assumption provides a lower bound in designing the hybrid system and leads to conservative design. The advantage of the simple analytical model is the ease with which one can assess the overall response in a design without having to consider the detailed hybrid behavior. In the detailed finite element analyses, the Johnson-Cook constitutive model was used to simulate plasticity in the aluminum, which is suitable for metals subjected to large strains, high strain rates, and high temperatures. CFRP and epoxy were modeled by shell elements and cohesive elements, respectively. Simulations were run to obtain the dynamic displacement time history in a pulse loading scenario. This dynamic displacement time history is arguably the most important parameter in blast resistant design. Three different failure modes—fiber rupture (FR), metal-fiber debonding (MFD), and interlaminar rupture (ILD)—are discussed in the paper. FR and ILD are prevalent in impulsive tests, while MFD is not so common. The parametric studies conducted showed that the thickness of the CFRP patch is an important factor that influences the results. An increasing number of CFRP layers increases the dynamic load bearing capacity of the hybrid beam and reduces the corresponding blasted induced maximum deformation.

Conflict of Interests

The authors declare no possible conflict of interests.

Acknowledgments

The authors gratefully acknowledge the financial support from the National Nature Science Foundation of China (nos. 51079127, 51179171, and 51279180) and the National Basic Research Programme of China (2013CB035901).

References

- [1] P. A. Buchan and J. F. Chen, "Blast resistance of FRP composites and polymer strengthened concrete and masonry structures—a state-of-the-art review," *Composites B*, vol. 38, no. 5-6, pp. 509–522, 2007.
- [2] X.-L. Zhao and L. Zhang, "State-of-the-art review on FRP strengthened steel structures," *Engineering Structures*, vol. 29, no. 8, pp. 1808–1823, 2007.
- [3] G. S. Langdon, W. J. Cantwell, and G. N. Nurick, "Localised blast loading of fibre-metal laminates with a polyamide matrix," *Composites B*, vol. 38, no. 7-8, pp. 902–913, 2007.
- [4] D. Schnerch and S. Rizkalla, "Flexural strengthening of steel bridges with high modulus CFRP strips," *Journal of Bridge Engineering*, vol. 13, no. 2, pp. 192–201, 2008.
- [5] ACI Committee 440, *Guide for the Design and Construction of Externally Bonded FRP Systems for Strengthening Concrete Structures*, American Concrete Institute, Farmington Hills, Mich, USA, 2002.
- [6] J. Teng, *FRP-Strengthened RC Structures*, John Wiley & Sons, 2002.
- [7] L. C. Hollaway, "A review of the present and future utilisation of FRP composites in the civil infrastructure with reference to their important in-service properties," *Construction and Building Materials*, vol. 24, no. 12, pp. 2419–2445, 2010.
- [8] M. R. Bambach, X. L. Zhao, and H. Jama, "Energy absorbing characteristics of aluminium beams strengthened with CFRP subjected to transverse blast load," *International Journal of Impact Engineering*, vol. 37, no. 1, pp. 37–49, 2010.
- [9] T.-C. Nguyen, Y. Bai, X.-L. Zhao, and R. Al-Mahaidi, "Mechanical characterization of steel/CFRP double strap joints at elevated temperatures," *Composite Structures*, vol. 93, no. 6, pp. 1604–1612, 2011.
- [10] D. Linghoff, M. Al-Emrani, and R. Kliger, "Performance of steel beams strengthened with CFRP laminate—part 1: laboratory tests," *Composites B*, vol. 41, no. 7, pp. 509–515, 2010.
- [11] M. R. Bambach, "Axial capacity and crushing behavior of metal-fiber square tubes—steel, stainless steel and aluminum with CFRP," *Composites B*, vol. 41, no. 7, pp. 550–559, 2010.
- [12] B. Lanier, D. Schnerch, and S. Rizkalla, "Behavior of steel monopoles strengthened with high-modulus CFRP materials," *Thin-Walled Structures*, vol. 47, no. 10, pp. 1037–1047, 2009.
- [13] T. S. P. Austin, M. M. Singh, P. J. Gregson, and P. M. Powell, "Characterisation of fatigue crack growth and related damage mechanisms in FRP-metal hybrid laminates," *Composites Science and Technology*, vol. 68, no. 6, pp. 1399–1412, 2008.
- [14] P. Colombi, "Reinforcement delamination of metallic beams strengthened by FRP strips: fracture mechanics based approach," *Engineering Fracture Mechanics*, vol. 73, no. 14, pp. 1980–1995, 2006.
- [15] T. J. Stratford and J. F. Chen, "Designing for tapers and defects in FRP-strengthened metallic structures," in *Proceedings of the International Symposium on Bond Behaviour of FRP in Structures (BBFS '05)*, pp. 453–458, Iific Secretariat, Hong Kong, 2005.
- [16] S. Fawzia, R. Al-Mahaidi, X. L. Zhao, and S. Rizkalla, "Strengthening of circular hollow steel tubular sections using high modulus CFRP sheets," *Construction and Building Materials*, vol. 21, no. 4, pp. 839–845, 2007.
- [17] M. R. Bambach, H. H. Jama, and M. Elchalakani, "Axial capacity and design of thin-walled steel SHS strengthened with CFRP," *Thin-Walled Structures*, vol. 47, no. 10, pp. 1112–1121, 2009.
- [18] S. Fawzia, X.-L. Zhao, and R. Al-Mahaidi, "Bond-slip models for double strap joints strengthened by CFRP," *Composite Structures*, vol. 92, no. 9, pp. 2137–2145, 2010.
- [19] J. Haedir, M. R. Bambach, X.-L. Zhao, and R. H. Grzebieta, "Strength of circular hollow sections (CHS) tubular beams externally reinforced by carbon FRP sheets in pure bending," *Thin-Walled Structures*, vol. 47, no. 10, pp. 1136–1147, 2009.
- [20] M. A. Youssef, "Analytical prediction of the linear and nonlinear behaviour of steel beams rehabilitated using FRP sheets," *Engineering Structures*, vol. 28, no. 6, pp. 903–911, 2006.
- [21] J. Deng, M. M. K. Lee, and S. S. J. Moy, "Stress analysis of steel beams reinforced with a bonded CFRP plate," *Composite Structures*, vol. 65, no. 2, pp. 205–215, 2004.
- [22] J. Deng, M. M. K. Lee, and S. Li, "Flexural strength of steel-concrete composite beams reinforced with a prestressed CFRP plate," *Construction and Building Materials*, vol. 25, no. 1, pp. 379–384, 2011.
- [23] N. Jones, *Structural Impact*, Cambridge University Press, 1997.

- [24] N. Jones, "A theoretical study of the dynamic plastic behavior of beams and plates with finite-deflections," *International Journal of Solids and Structures*, vol. 7, no. 8, pp. 1007–1029, 1971.
- [25] G. R. Cowper and P. S. Symonds, "Strain-hardening and strain-rate effects in the impact loading of cantilever beams," Brown University Division of Applied Mathematics Report 28, 1957.
- [26] S. R. Bodner and P. S. Symonds, "Experimental and theoretical investigation of the plastic deformation of cantilever beams subjected to impulsive loading," *Journal of Applied Mechanics*, vol. 29, p. 719, 1962.
- [27] H. Jama, M. Bambach, R. Grzebieta, and X.-L. Zhao, "Numerical modelling of simply supported square tubular beams subjected to a uniform blast load," in *Proceedings of the 19th Australasian Conference on the Mechanics of Structures and Materials (ACMSM '19)*, pp. 777–782, Christchurch, New Zealand, December 2006.
- [28] H. H. Jama, M. R. Bambach, G. N. Nurick, R. H. Grzebieta, and X.-L. Zhao, "Numerical modelling of square tubular steel beams subjected to transverse blast loads," *Thin-Walled Structures*, vol. 47, no. 12, pp. 1523–1534, 2009.
- [29] S. C. K. Yuen and G. N. Nurick, "Experimental and numerical studies on the response of quadrangular stiffened plates. Part I: subjected to uniform blast load," *International Journal of Impact Engineering*, vol. 31, no. 1, pp. 55–83, 2005.
- [30] D. Karagiozova, G. N. Nurick, and S. Chung Kim Yuen, "Energy absorption of aluminium alloy circular and square tubes under an axial explosive load," *Thin-Walled Structures*, vol. 43, no. 6, pp. 956–982, 2005.
- [31] V. H. Balden and G. N. Nurick, "Numerical simulation of the post-failure motion of steel plates subjected to blast loading," *International Journal of Impact Engineering*, vol. 32, no. 1–4, pp. 14–34, 2006.
- [32] G. R. Johnson and W. H. Cook, "Fracture characteristics of three metals subjected to various strains, strain rates, temperatures and pressures," *Engineering Fracture Mechanics*, vol. 21, no. 1, pp. 31–48, 1985.
- [33] G. R. Johnson and W. H. Cook, "A constitutive model and data for metals subjected to large strains, high strain rates and high temperatures," in *Proceedings of the 7th Symposium on Ballistic*, pp. 541–547, Hague, The Netherlands, 1983.
- [34] N. K. Gupta, M. A. Iqbal, and G. S. Sekhon, "Experimental and numerical studies on the behavior of thin aluminum plates subjected to impact by blunt- and hemispherical-nosed projectiles," *International Journal of Impact Engineering*, vol. 32, no. 12, pp. 1921–1944, 2006.
- [35] ABAQUS, "Abaqus 6. 11 User Documentation," Dessault Systems, 2011.
- [36] O. Pantalé, J.-L. Bacaria, O. Dalverny, R. Rakotomalala, and S. Caperaa, "2D and 3D numerical models of metal cutting with damage effects," *Computer Methods in Applied Mechanics and Engineering*, vol. 193, no. 39–41, pp. 4383–4399, 2004.
- [37] Z. Hashin, "Failure criteria for unidirectional fiber composites," *Journal of Applied Mechanics, Transactions ASME*, vol. 47, no. 2, pp. 329–334, 1980.
- [38] A. Matzenmiller, J. Lubliner, and R. L. Taylor, "A constitutive model for anisotropic damage in fiber-composites," *Mechanics of Materials*, vol. 20, no. 2, pp. 125–152, 1995.
- [39] C. G. Dávila and P. P. Camanho, "Failure criteria for FRP laminates in plane stress," NASA TM 212663, 2003.
- [40] M. Elices, G. V. Guinea, J. Gómez, and J. Planas, "The cohesive zone model: advantages, limitations and challenges," *Engineering Fracture Mechanics*, vol. 69, no. 2, pp. 137–163, 2001.
- [41] X.-K. Zhu and J. A. Joyce, "Review of fracture toughness (G, K, J, CTOD, CTOA) testing and standardization," *Engineering Fracture Mechanics*, vol. 85, pp. 1–46, 2012.
- [42] D. G. Dixon, "Spall failure in a carbon fibre reinforced thermoplastic composite," *Journal of Materials Science Letters*, vol. 9, no. 5, pp. 606–608, 1990.
- [43] J. S. Humphreys, "Plastic deformation of impulsively loaded straight clamped beams (Plastic deformation of flat steel beams impulsively loaded by sheet explosive)," *ASME Transactions Series E-Journal of Applied Mechanics*, vol. 32, pp. 7–10, 1965.
- [44] H. Zhu, L. Zhu, and J. H. Chen, "Influence of stress triaxiality and strain rate on the mechanics behavior of 6063 aluminum alloy and material characterization," *Journal of Materials Science & Engineering*, vol. 25, no. 3, pp. 358–362, 2007.



Hindawi

Submit your manuscripts at
<http://www.hindawi.com>

